

Combination of hollow-core sapphire waveguide and immersion lens for ultra-high resolution THz endoscopy

© A.S. Kucheryavenko¹, V.A. Zhelnov¹, N.V. Chernomyrdin², V.N. Kurlov¹, K.I. Zaytsev², G.M. Katyba¹

¹ Osipyan Institute of Solid State Physics RAS, Chernogolovka, Russia

² Prokhorov Institute of General Physics, Russian Academy of Sciences, Moscow, Russia

e-mail: ans.kucher@mail.ru

Received February 07, 2023

Revised February 13, 2023

Accepted February 16, 2023.

The development of terahertz (THz) imaging methods is hampered by the low spatial resolution of traditional diffraction-limited imaging systems, mainly due to the large wavelength of used radiation (from a few of mm to tens of μm). To solve this problem, we have proposed a new method of THz endoscopy with subwavelength spatial resolution, which is designed to study hard-to-reach areas of living organisms *in vivo*. A hollow-core sapphire tube with polytetrafluoroethylene outer coating is used as a waveguide, in which the antiresonant principle of radiation transmission is implemented. The waveguide and the immersion lens are optimized to provide high optical characteristics in a given wavelength range to ensure the best focusing. Two immersion lenses made of sapphire and silicon were developed and fabricated, which were then mounted on plane-parallel windows fixed on the rear end of the waveguide. The study of the field intensity distribution on the shadow side of the glqq waveguide–lens“system revealed a focal spot diameter of $\simeq 0.2\lambda$ in the case of a lens made of sapphire and $\simeq 0.3\lambda$ in the case of a lens made of crystal silicon at a wavelength $\lambda = 500\ \mu\text{m}$, which significantly exceeds the Abbe diffraction limit. This agrees with our numerical predictions and demonstrates the promise of using the proposed endoscope for measurements with subwavelength resolution.

Keywords: terahertz radiation, terahertz imaging, endoscopy, subwavelength spatial resolution, Abbe diffraction limit, solid immersion effect.

DOI: 10.61011/EOS.2023.06.56674.123-23

Introduction

Various applications using terahertz (THz) radiation have the potential to be applied in various socially and industrially important areas [1], such as medical diagnostics [2] and therapy [3], non-destructive testing of materials [4], quality control of medicines [5] and foodstuffs [6], as well as safety-related tasks [7]. However, despite the rapid development of THz technologies, their capabilities are limited to a significant extent by a number of problems in the field of THz optics hardware components, two main of which will be in the focus of this study.

The first challenge is the lack of commercially available waveguides and fibers for delivering radiation of this range to hard-to-reach objects of study and/or targets [8]. By now, there is a fairly large list of designs that use various physical mechanisms for transmitting radiation, for example, plane-parallel [9] or tubular [10] metal waveguides, polymer antiresonant or photonic-crystal waveguides [11,12], step index fibers [13], porous fibers [14] and plasmonic waveguides [15,16]. However, in many respects, the transmission of THz radiation over long distances with the help of above-listed technical means is difficult due to large dispersion, radiation losses during propagation, or radiation losses during input/output. In addition, many waveguides do not always have sufficient technological reliability, and also have low thermal, radiation and chemical resistance [17].

These factors complicate the practical application of THz waveguides, for example, the measurement of hard-to-reach objects in healthcare or industry [17,18].

To cope with this challenge, it was previously proposed to transmit THz radiation using profiled sapphire crystals grown by the edge-defined, film-fed growth (EFG) method [19]. The combination of the unique physical and chemical properties of sapphire (high refractive index and relatively low absorption coefficient in the THz range, high mechanical strength, chemical inertness, thermal and radiation resistance) with the possibility of growing profiled crystals with a complex cross-sectional geometry and optical quality of crystals in their body and on the surface makes such sapphire waveguides an excellent supplement to the pool of THz range hardware components. In previous studies, the authors have developed and fabricated hollow sapphire antiresonant waveguides [20] and photonic-crystal waveguides [17] for low-loss radiation transmission, flexible fibers [21,22] and fiber bundles [23,24] for imaging with subwavelength resolution.

The second challenge is the low spatial resolution of traditional lens and mirror focusing optical elements, which is restricted by the diffraction limit of spatial resolution (the so-called Abbe limit). Even for a diffraction-limited THz optical system with the highest possible numerical aperture, the spatial resolution is $\simeq 0.5\lambda$ (where λ is the radiation wavelength in free space)

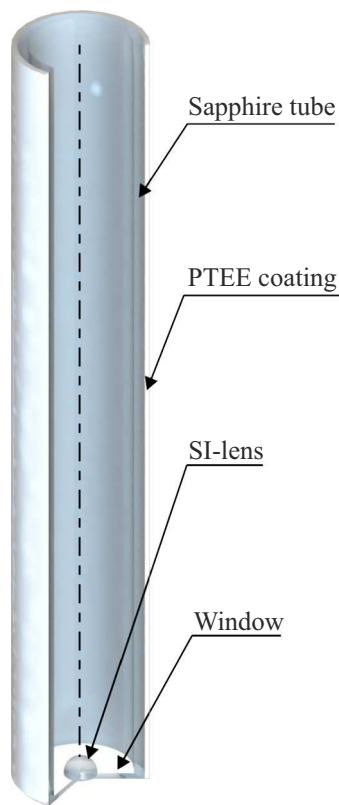


Figure 1. Schematic diagram of a THz endoscope based on a hollow antiresonant waveguide. At the output of the waveguide, a plane-parallel window is installed, on which an immersion lens is fixed.

and is usually a few hundred microns (or even a few millimeters) due to the long wavelengths in the THz range [25].

Currently, there are several methods of THz imaging with spatial resolution exceeding the Abbe limit. For example, the THz scanning probe near-field microscopy is able to distinguish field inhomogeneities with a strongly subwavelength spatial resolution ($\sim 10^{-3} - 10^{-4}\lambda$) [26,27]. Unfortunately, these methods have a limited field of view, low speed and extremely low energy efficiency, which means that they require the use of powerful sources and sensitive THz radiation detectors. The solid state immersion method is a good alternative to near-field scanning probes because it provides a trade-off between resolution, operation speed and energy efficiency [28–30]. The latest results are indicative of the possibility to determine the distribution of the optical properties of the sample over the focal plane with a resolution of up to 0.15λ . And due to the absence of subwavelength elements (such as probes and diaphragms) in the optical scheme, a much higher energy efficiency is achieved than in near-field imaging methods.

The purpose of this study was to develop and test a new method of THz endoscopy with a spatial resolution exceeding the Abbe limit. Schematic diagram of a THz endoscope, which combines the possibility of

transmitting radiation with low losses using a sapphire waveguide and the localization of waveguide modes at the output by a solid immersion (SI) lens, is shown in Fig. 1. The lens is located on the inner side of the waveguide and is fixed in the center of a plane-parallel window. The waveguide is made of a sapphire ($\alpha\text{-Al}_2\text{O}_3$) tube with polytetrafluoroethylene (PTFE) coating [31]. Materials with a high refractive index and, at the same time, low absorption were selected for the manufacture of the „SI-lens–plane-parallel window“ assembly: high-resistivity float-zone silicon — HRFZ-Si) and sapphire ($n_{\text{HRFZ-Si}} \approx 3.41$ and $n_{\text{sapphire}} \approx 3.07$ for a frequency of $\nu = 1$ THz). The intensity distribution of the THz field at the output of the endoscope was recorded using a scanning system, where a backward-wave oscillator (BWO) was used as a source of continuous radiation with a maximum output power at the incident radiation wavelength of $\lambda = 500 \mu\text{m}$.

The measurement results show that a focal spot of intensity with spatial dimensions of $\approx 0.2\lambda$ is formed at the output of the THz endoscope, which is consistent with numerical predictions and confirms its ability to ensure a subwavelength spatial resolution. The developed endoscope is a promising tool for use in studies of soft biological tissues and aggressive media.

Development and fabrication of a THz waveguide based on a hollow sapphire tube

For the tasks of THz endoscopy, it was necessary to find a trade-off between minimizing the size of the entire system (in particular, the diameter of the waveguide) and maintaining the energy efficiency. In order to optimize the cross section of an antiresonant waveguide based on a polymer-coated sapphire tube, a series of numerical calculations of waveguide characteristics for various cross-sectional geometries was carried out. As a result, a sapphire tube with inner and outer diameters of 6.3 and 7.6 mm, respectively, was chosen, the c axis of the sapphire crystal was directed parallel to the optical axis of the waveguide, and the PTFE coating thickness was 0.4 mm. With the above-specified geometry parameters, the waveguide will transmit radiation in a quasi-single-mode operation, which will allow only the fundamental mode to be taken into account in the modeling. The polymer coating is a heat-shrinkable tube; to ensure a uniform and tight fit of the shell to the sapphire surface, the workpiece was held for 30 min in a muffle furnace at a temperature of 350°C .

It is worth noting that a similar structure of antiresonant waveguide was described in the earlier study of the authors [20], so here the detailed description of the process of manufacturing such a tube by the EFG method is omitted.

Fig. 2, *a* shows a photo of the fabricated waveguide with a length of 50 mm, and Fig. 2, *b* shows the intensity

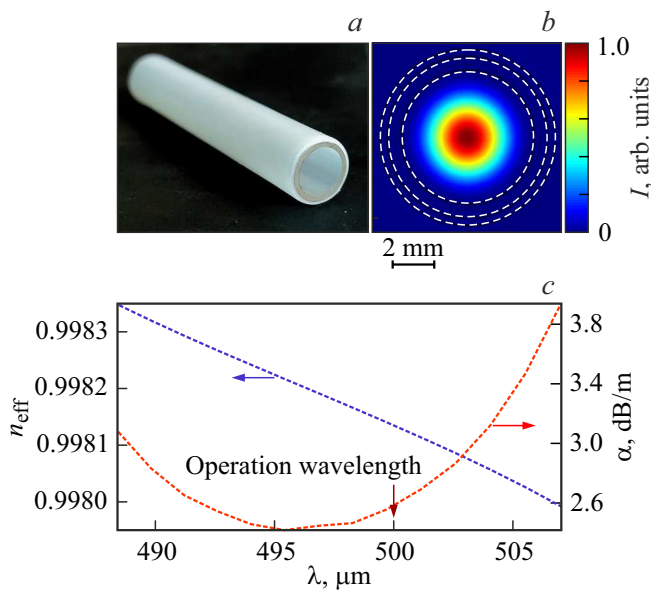


Figure 2. Hollow antiresonant THz waveguide based on a PTFE-coated sapphire tube. (a) Photo of the waveguide. (b) Intensity of the $I \propto |\mathbf{E}|^2$ mode in the waveguide cross section at $\lambda = 500 \mu\text{m}$. (c) FDE numerical modeling data for the effective refractive index n_{eff} and propagation loss α (in terms of power) of the fundamental mode.

distribution of the fundamental mode $I \propto |\mathbf{E}|^2$ (where \mathbf{E} is electric field vector) in the waveguide cross-section.

Fig. 2, c shows the results of numerical modeling of the optical characteristics of the waveguide fundamental mode obtained using the finite-difference eigenmode (FDE) method [32] in the ANSYS Mode software. Dependences of the effective refractive index $n_{\text{eff}}(\lambda)$ (the real part of the complex refractive index) and the intensity attenuation coefficient $\alpha(\lambda)$ for the fundamental mode are shown. The modeling was carried out taking into account both the THz optical properties of sapphire and various technological limitations imposed due to the use of the EFG method. Birefringence in sapphire crystals was taken into account by determining the dielectric properties of the medium in tensor form, however, as can be seen from Fig. 2, b, almost all of the mode energy is localized in the hollow channel, which minimizes the effect of crystal anisotropy on the properties of the waveguide [17,19,33].

When a THz wave propagates from a BWO-generator ($\lambda = 500 \mu\text{m}$), the losses are $\alpha \approx 2.6 \text{ dB/m}$, which makes it possible to consider such a waveguide as weakly absorbing. Also, it is worth to note that the mode has a rather large area ($> \lambda^2$), and the field distribution is of Gaussian shape (the mode intensity monotonically decreases from the optical axes), which allowed us to model an SI-lens with a diameter of no more than 2–3 mm regardless of the waveguide and consider the incident wave of the focusing element as a plane wave. Taking into account the above-mentioned considerations, a conclusion can be made that the intensity level of the signal transmitted through a relatively short

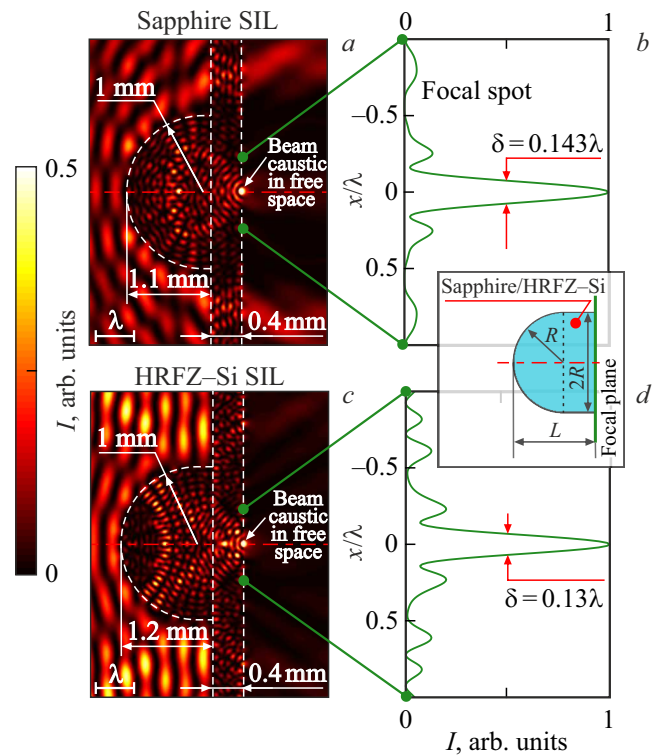


Figure 3. FDTD modeling of SI-lenses made of sapphire and silicon at $\lambda = 500 \mu\text{m}$. (a, c) Intensity of the $I \propto |\mathbf{E}|^2$ field in the axial cross-section of SI-lenses made of sapphire and silicon, (b, d) focal spot on the shadow side (in the free space), respectively.

waveguide (in our case it is $l = 50 \text{ mm}$) will be sufficient for successful recording of the field distribution at the waveguide output.

Development of the SI-lens design

The SI lens is a hemisphere aligned with a cylinder (the so-called „bullet“ geometry), where the radius of the spherical surface is R , the diameter of the cylinder is $2R$, and the total thickness is L . This geometry was chosen to achieve a greater ease of fabrication of the immersion element. The process of interaction between the SI-lens and a plane TEM-polarized wave was modeled by the finite-difference time domain (FDTD) method [34]. To reduce the computational complexity, the modeling of cylindrical (2D) optical elements was used with the cross-section equal to the cross-section of axially symmetric elements (3D), and a scattered field with TM-polarization was considered. In [34] such a 2D approximation gave quite relevant predictions for 3D SI-lens systems.

As a result of a series of FDTD modeling sessions, geometric parameters of the SI-lens were optimized. First, for the „bullet“ type geometry (inset in Fig. 3) the dependence of the spatial resolution on the radius of the spherical surface and base R and thickness L was studied.

Due to the fact that the SI-lens is supposed to be fixed at the center of a plane-parallel window at the waveguide output, then the influence of such a window on the resolution of the system was checked. Namely, an additional series of calculations was carried out, in which the thickness of the SI-lenses was reduced by a certain value and increased to the initial value of L by a plane-parallel window of the same material. Fig. 3 shows the FDTD modeling data for the intensity distribution of the THz field $I \propto |\mathbf{E}|^2$ in the axial cross-section of the modified SI-lens design (Fig. 3, *a, c*) and the focal spot on the shadow side of the SI-lens made of sapphire and silicon, respectively (Fig. 3, *b, d*). The diameter of the focal spot behind the lens was considered as the spatial resolution δ (δ was equal to the full width at half maximum (FWHM) of the intensity amplitude).

Fig. 4 shows the results of optimizing the geometry of a SI-lens made of sapphire and silicon at an incident radiation wavelength of $\lambda = 500 \mu\text{m}$. The lens radius R was considered in the range from 0.1 to 5 mm and the reduced thickness $L/(2R)$ was from 0.2 to 1 (Fig. 4, *a, c*). Based on the results of numerical analysis, both the HRFZ-Si SI-lens with $R = 1 \text{ mm}$ and $L = 1.6 \text{ mm}$ parameters, and the sapphire SI-lens with $R = 1 \text{ mm}$ and $L = 1.5 \text{ mm}$ demonstrated the focusing of radiation into a very small focal spot located immediately behind the lens, which means a record low spatial resolution ($\delta_{\text{HRFZ-Si}} = 0.136\lambda$ and $\delta_{\text{Sapphire}} = 0.152\lambda$). In this case, both lenses have a diameter of 2 mm, which is small enough to fit inside the waveguide. They can also be made by conventional machining of a massive crystal. The panels in Fig. 4, *b, d* show the results of studying the dependence of the spatial resolution δ on the thickness of a plane-parallel window using FDTD-modeling. As mentioned earlier, the thickness of the „lens-window“ assembly remained unchanged, and the window thickness varied from 0.1 to 1 mm. The red dashed line shows the resolution value δ for the initial immersion lens. For both sapphire and silicon SI-lenses, reducing the lens thickness by 0.4 mm and supplementing it with a plane-parallel window to the original thickness made it possible to further reduce the beam caustic formed on the rear surface of the plane-parallel windows.

Thus, it follows from the results of the numerical analysis that the configurations of SI-lenses used are optimal and provide subwavelength localization of the field at a small distance behind the endoscope ($\ll \lambda$), where the focal plane almost coincides with the rear (flat) surface of the SI-lenses.

Experimental characterization of the THz endoscope spatial resolution

To experimentally determine the resolution of the imaging system on the basis of the developed THz endoscope and the BWO, an experimental setup was assembled, the schematic diagram of which is shown in Fig. 5, *a*. A Golay cell (an optoacoustic receiver) was chosen as the detector

of the transmitted intensity. A mechanical chopper was used to modulate the intensity of the transmitted THz wave. To visualize the field distribution in the focal plane (immediately behind the plane-parallel window), a scanning diaphragm with a diameter of λ was used.

It should be noted that the proposed experimental imaging system will have a spatial resolution equal to the diameter of the scanning aperture, i.e. will be equal to λ . This is insufficient for a quantitative evaluation of the subwavelength focal spot size (and, accordingly, the point spread function of the system). For this purpose, another measurement scheme was used, which involves 1D-scanning using a test object with a sharp change in the spatial distribution of the reflection coefficient [23,24,28,29,34].

The developed SI-lenses were fabricated and connected to the waveguide (Fig. 5, *b*). First, the lenses were attached to plane-parallel windows by polystyrene glue (Fig. 5, *c, d*), then aperture diaphragms made of a conductive polymer on a 3D printer and having an inner diameter slightly larger than the diameter of the SI-lens were mounted on the resulting assemblies (Fig. 5, *b*). The outer edge of the diaphragm is a cylinder with a diameter exactly equal to the outer diameter of the waveguide (it is needed as a fixator at the end of the waveguide for the focusing element). The diaphragm is needed to shutoff the peripheral part of the fundamental mode (and higher-order modes) and to make it easier to replace lenses during experiments. Other options for assembling the „lens-window“ assembly at the end of the waveguide are also possible: gluing the window to the end or manufacturing a monolithic „tube-window“ assembly directly in the process of growing a sapphire crystal using the EFG method [35].

2D and 1D visualization methods were used to check the value of the spatial resolution of the endoscope predicted in the course of numerical modeling, as well as to visualize the intensity distribution at the output end of the endoscope.

In the case of 2D visualization, raster scanning of the wavefront in the focal plane was carried out by a diaphragm with a diameter of λ , which was rigidly fixed on the Golay cell and moved together with it on linear motorized platforms under program control (Fig. 5, *e*).

In the case of 1D scanning, a metal blade was moved in the focal plane in the direction parallel or perpendicular to the polarization of the incident wave. The Golay cell was located motionless and detected the change in the intensity of the transmitted radiation depending on the position of the blade (Fig. 5, *f*). From the value of the recorded first derivative of the field intensity as a function of the blade tip coordinate (i.e., the point spread function of the imaging system) a conclusion can be made about the spatial dimensions of the focal spot.

Fig. 6, *a* shows the experimental 2D image of the THz field intensity $I(x, y)$ immediately behind the rear end of the waveguide without a lens, and the panels (*b, c*) show cross-sections in perpendicular (*OX*) and parallel (*OY*) directions relative to the radiation polarization, respectively.

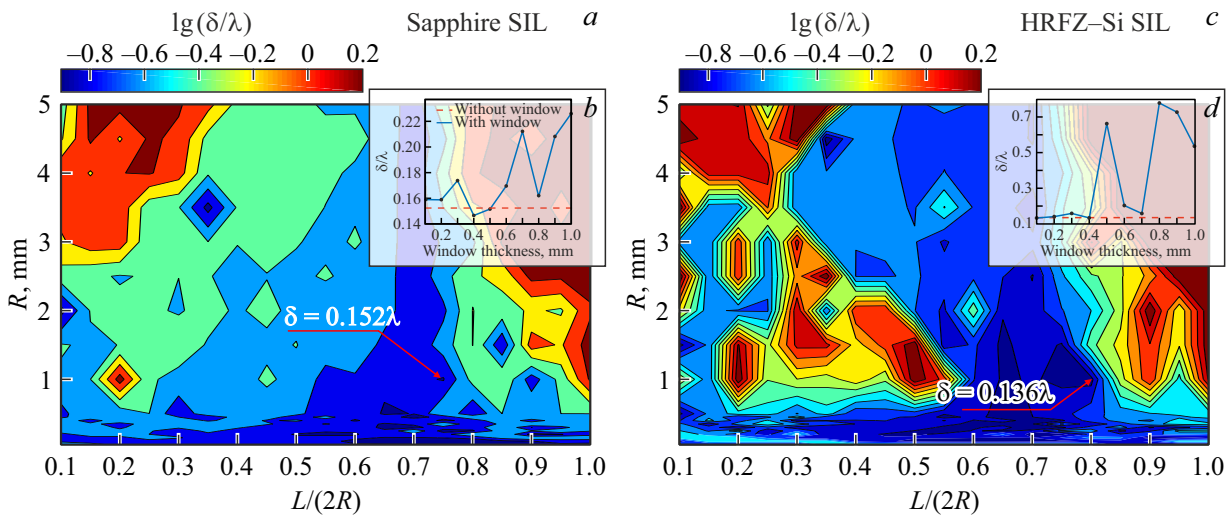


Figure 4. Numerical FDTD-optimization of „bullet“ SI-lenses at $\lambda = 500\mu\text{m}$. (a, c) Resolution of SI-lenses made of sapphire and silicon δ as a function of radius R and normalized thickness $L/(2R)$, normalized to the radiation wavelength λ ; (b, d) Resolution of SI-lenses made of sapphire and silicon δ , normalized to the radiation wavelength λ depending on the thickness replaced by a plane-parallel window. The red marker in (a, c) shows the resolution of the SI-lens geometries selected for further experiments.

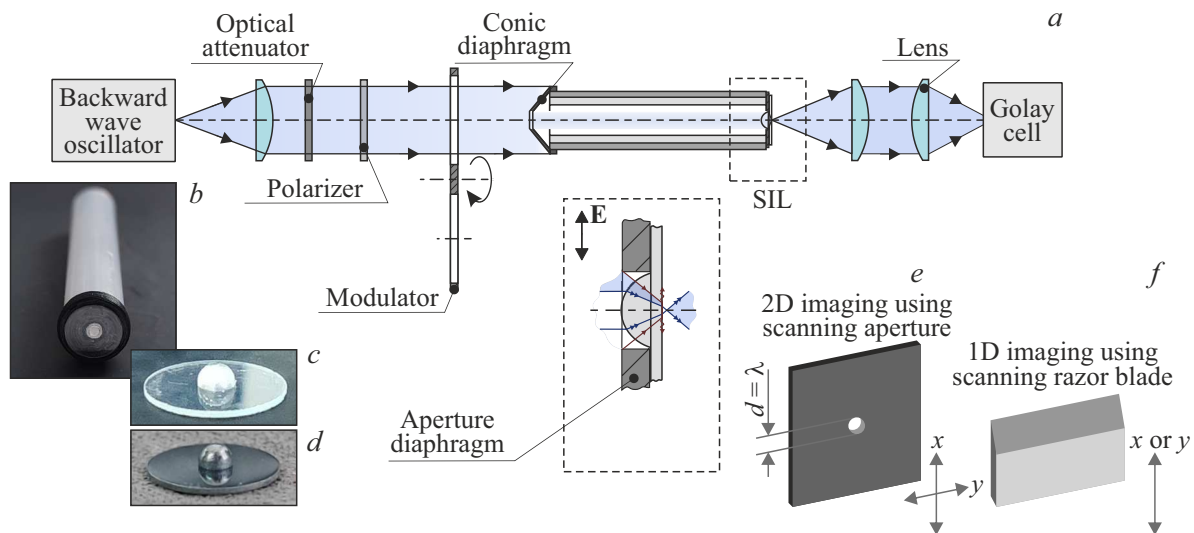


Figure 5. (a) Schematic diagram of the experimental setup for testing the resolution of the THz endoscope, operating in the „transmission“ mode. (b–d) Photo of the THz endoscope with a SI-lens mounted in a polymer diaphragm holder and separate photos of sapphire and silicon SI-lenses after gluing the hemisphere and window. (e–f) Illustration of two approaches to visualize the intensity of the THz field at the output of a THz endoscope using a scanning diaphragm and a sharp metal blade, respectively.

As predicted earlier (Fig. 2, b), for an „empty“ waveguide, the intensity of the fundamental mode decreases monotonically from the center to the periphery of the cross-section, and the mode size at half-height is $\approx 3\lambda$ (Fig. 6, b, c). These results confirmed the ability of an antiresonant hollow core waveguide to transmit radiation with a wavelength of λ . However, it is clear that a waveguide without the SI-lens is not suitable for the tasks, where the radiation needs to be focused into a subwavelength spot.

Fig. 6, d shows the experimentally recorded image of the THz field immediately behind the endoscope. Visualization

was carried out using a scanning diaphragm. This image shows a much more local intensity spot, confirming that the fundamental mode is focused by the SI-lens. However, the THz image obtained in this way is limited by the resolution of the scanning aperture with a diameter of λ , which is ≥ 5 times higher than the expected subwavelength resolution of the imaging system.

To quantify the parameters of the focal spot of the SI-lens, 1D scanning with a metal blade was carried out [23,24,28,29,34]. The scattering function of the system is defined as the first derivatives of the THz field intensity

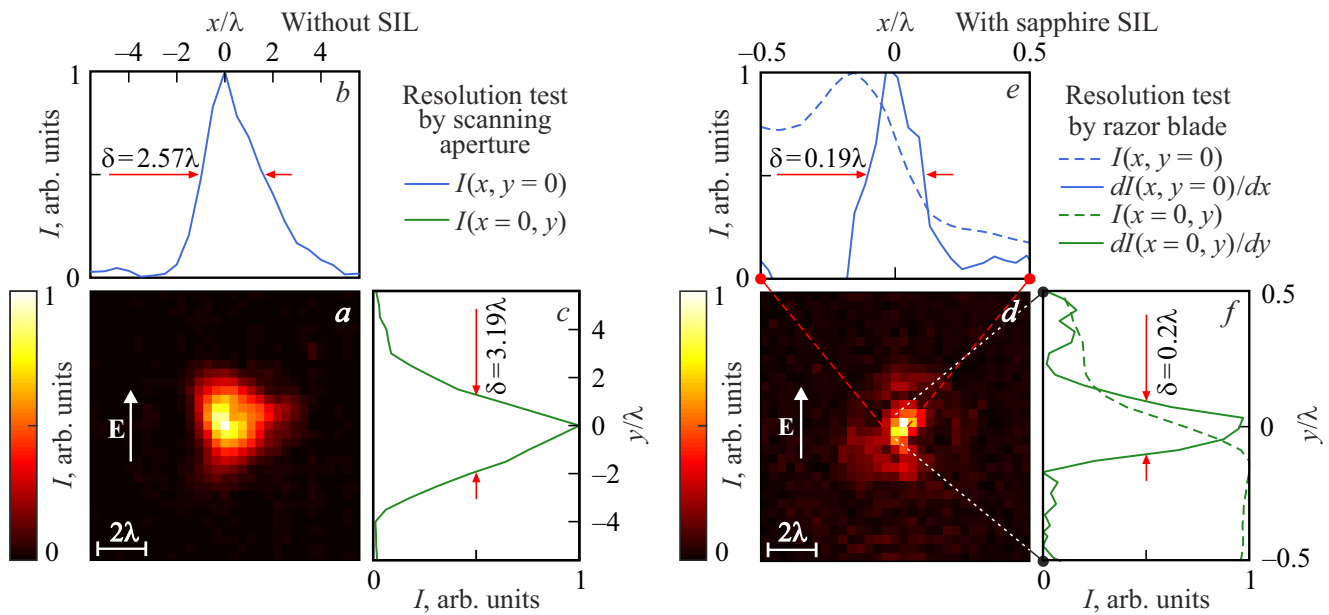


Figure 6. Visualization of the THz field intensity $I(x, y)$ behind the THz endoscope. (a–c) Field intensity behind the waveguide without a SI-lens, as well as its cross-sections along the OX and OY axes, obtained by scanning with an aperture of a diameter of λ . (d) Field intensity immediately behind the output end of the THz endoscope, obtained by scanning with an aperture of a diameter of λ . (f, g) Cross-sections of the field intensity ($I(x)$ and $I(y)$) along the OX and OY axes obtained by scanning with a metal blade, as well as the assumed point spread functions ($dI(x)/dx$ and $dI(y)/dy$).

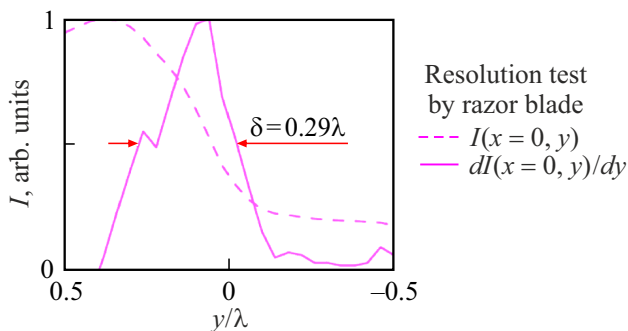


Figure 7. OY cross-section of the field intensity behind the waveguide - silicon SI-lens system ($I(y)$), obtained by scanning with a metal blade, as well as the assumed scattering function ($dI(y)/dy$).

cross-sections along the OX and OY axes passing through the central peak (Fig. 6, f, g, Fig. 7, b, c).

In the case of a SI-lens made of sapphire, the focal spot has subwavelength dimensions, i.e. 0.19λ and 0.2λ in the directions of OX and OY , respectively, which generally agrees with numerical predictions (Fig. 3, d). The observed discrepancy $< 25\%$ between modeling predictions and experimental data may arise due to discrepancies in physical processes in a real 3D optical system compared to the 2D modeled optical system, the influence of field re-reflections from a plane-parallel window and waveguide

walls, as well as residual misalignments of the experimental setup.

Despite the observed ≈ 15 -times increase in the resolution for the waveguide in the case of using a sapphire SI-lens, the resulting energy efficiency of the system decreases due to Fresnel reflection from the window surface and attenuation of the radiation in the sapphire. Indeed, the integral power of the beam behind the waveguide decreases, however, almost the same peak intensity is observed in a small region around the optical axis for the waveguide without (Fig. 6, a) and with a sapphire SI-lens (Fig. 6, d). The signal-to-noise ratio (SNR) for a THz endoscope with a sapphire SI-lens is ≈ 65 (Fig. 6, d), which is ≈ 1.6 times less as compared to a waveguide without a SI-lens installed on it (Fig. 6, a).

Fig. 7 shows the intensity cross-section obtained by 1D scanning and the assumed scattering function of the silicon SI-lens; the spatial resolution evaluation showed $\delta = 0.29\lambda$, which exceeds the Abbe limit but differs by more than 2 times from the modeling predictions. For an endoscope with a silicon SI-lens, we have found a strong decrease in the SNR value, which did not allow us to perform 2D-visualization of the field intensity distribution in the focal plane. Probably, for this geometry, a higher manufacturing accuracy of the SI-lens and the plane-parallel window is required, as well as an additional correction of standing waves that arise between the back surface of the plane-parallel window and metal elements (the scanning diaphragm or the metal sharp blade).

Conclusion

The designed THz endoscope has the potential for a variety of THz applications, including probing and use in aggressive environments [17,19,35]. However, before its implementation in these complex fields, it is necessary to solve a number of research and engineering problems. The resolution, power efficiency and spectral bandwidth of our endoscope can be improved by optimizing the waveguide and SI-lens geometry. For example, its energy efficiency can be improved both through further optimization of the waveguide geometry and through the use of antireflection coatings on SI-lenses or microstructures (to reduce Fresnel losses) [36]. In addition, the modeling results are indicative that the high-resolution region is kept when the lens diameter R is increased to a few mm. This opens up opportunities for increasing the energy efficiency of the endoscope. Finally, for the development of THz probing systems, it seems important to combine the developed endoscope with devices based on the principles of continuous or pulsed THz spectroscopy for remote quantitative evaluation of the optical properties of the analyte [30], while for the tasks of THz therapy it is necessary to test it together with powerful sources of THz radiation [3].

Conflict of interest

The authors declare that they have no conflict of interest.

References

- [1] H. Guerboukha, K. Nallappan, M. Skorobogatiy. *Adv. Opt. Photonics*, **10** (4), 843 (2018). DOI: 10.1364/AOP.10.000843
- [2] Z. Yan, L.-G. Zhu, K. Meng, W. Huang, Q. Shi. *Trends Biotechnol.*, **40** (7), 816 (2022). DOI: 10.1016/j.tibtech.2021.12.002
- [3] O.P. Cherkasova, D.S. Serdyukov, E.F. Nemova, A.S. Ratushnyak, A.S. Kucheryavenko, I.N. Dolganova, G. Xu, M. Skorobogatiy, I.V. Reshetov, P.S. Timashev, I.E. Spektor, K.I. Zaytsev, V.V. Tuchin. *J. Biomed. Opt.*, **26** (09), (2021). DOI: 10.1117/1.JBO.26.9.090902
- [4] C.D. Stoik, M.J. Bohn, J.L. Blackshire. *Opt. Express*, **16** (21), 17039 (2008). DOI: 10.1364/OE.16.017039
- [5] S. Zhong, H. Shen, Y.-C. Shen, J.A. Zeitler, L. Ho, M. Evans, P.T. Taday, M. Pepper, T. Rades, K.C. Gordon, R. Muller, P. Kleinebudde. In: *2009 34th International Conference on Infrared, Millimeter, and Terahertz Waves (IEEE, 2009)*, vol. 12, p. 1–2. DOI: 10.1109/ICIMW.2009.5324630
- [6] J.A. Zeitler, P.F. Taday, D.A. Newnham, M. Pepper, K.C. Gordon, T. Rades. *J. Pharmacy and Pharmacology*, **59** (2), 209 (2007). DOI: 10.1211/jpp.59.2.0008
- [7] K. Kawase, Y. Ogawa, Y. Watanabe, H. Inoue. *Opt. Express*, **11** (20), 2549 (2003). DOI: 10.1364/oe.11.002549
- [8] Md.S. Islam, C.M.B. Cordeiro, M.A.R. Franco, J. Sultana, A.L.S. Cruz, D. Abbott. *Opt. Express*, **28** (11), 16089 (2020). DOI: 10.1364/OE.389999
- [9] M. Mbonye, R. Mendis, D.M. Mittleman. *Appl. Phys. Lett.*, **95** (23), 233506 (2009). DOI: 10.1063/1.3268790
- [10] G. Xie, Y. Zhong, G. Li, C. She, X. Lu, F. Yue, S. Liu, C. Jing, Y. Cheng, J. Chu. *Results Phys.*, **19**, 103534 (2020). DOI: 10.1016/j.rinp.2020.103534
- [11] S.R. Andrews. *J. Phys. D: Appl. Phys.*, **47** (37), 374004 (2014). DOI: 10.1088/0022-3727/47/37/374004
- [12] G. Xu, K. Nallappan, Y. Cao, M. Skorobogatiy. *Sci. Rep.*, **12** (1), 4551 (2022). DOI: 10.1038/s41598-022-08334-6
- [13] S.P. Jamison, R.W. McGowan, D. Grischkowsky. *Appl. Phys. Lett.*, **76** (15), 1987 (2000). DOI: 10.1063/1.126231
- [14] B. Ung, A. Mazhorova, A. Dupuis, M. Roze, M. Skorobogatiy. *Opt. Express*, **19** (26), B848 (2011). DOI: 10.1364/OE.19.00B848
- [15] K. Wang, D.M. Mittleman. *J. Opt. Soc. Am. B*, **22** (9), 2001 (2005). DOI: 10.1364/JOSAB.22.002001
- [16] Y. Cao, K. Nallappan, G. Xu, M. Skorobogatiy. *Nature Communications*, **13** (1), 4090 (2022). DOI: 10.1038/s41467-022-31590-z
- [17] G.M. Katyba, K.I. Zaytsev, N. V. Chernomyrdin, I.A. Shikunova, G.A. Komandin, V.B. Anzin, S.P. Lebedev, I.E. Spektor, V.E. Karasik, S.O. Yurchenko, I.V. Reshetov, V.N. Kurlov, M. Skorobogatiy. *Adv. Opt. Mater.*, **6** (22), 1800573 (2018). DOI: 10.1002/adom.201800573
- [18] B. You, D.J. Monk, D.R. Walt, Z. Yang, M. Zhang, Y. Liao, Q. Tian, Q. Li, Y. Zhang, Z. Zhuang, E. Fabry, A. Albertazzi, A.C. Hofmann, A.V. Fantin, J.M.C. Santos, J.Y. Lu, C.M. Chiu, C.C. Kuo, C.H. Lai, H.C. Chang, Y.J. Hwang, C.L. Pan, C.K. Sun. *Opt. Exp.*, **24** (16), 18013 (2016). DOI: 10.1364/OE.24.018013
- [19] G.M. Katyba, K.I. Zaytsev, I.N. Dolganova, N.V. Chernomyrdin, V.E. Ulitko, S.N. Rossolenko, I.A. Shikunova, V.N. Kurlov. *Progress in Crystal Growth and Characterization of Materials*, **67** (3), 100523 (2021). DOI: 10.1016/j.pcrysgrow.2021.100523
- [20] G.M. Katyba, P.A. Chizhov, V.N. Kurlov, I.N. Dolganova, S.V. Garnov, K.I. Zaytsev, V.V. Bukin. *Opt. Express*, **30** (3), 4215 (2022). DOI: 10.1364/OE.447060
- [21] G.M. Katyba, D.G. Melikyants, N.V. Chernomyrdin, V.N. Kurlov, K.I. Zaytsev. *Opt. Eng.*, **60** (08), (2021). DOI: 10.1117/1.OE.60.8.082010
- [22] D.S. Ponomarev, D.V. Lavrukhin, N.V. Zenchenko, T.V. Frolov, I.A. Glinskiy, R.A. Khabibullin, G.M. Katyba, V.N. Kurlov, T. Otsuji, K.I. Zaytsev. *Opt. Lett.*, **47** (7), 1899 (2022). DOI: 10.1364/OL.452192
- [23] K.I. Zaytsev, G.M. Katyba, N.V. Chernomyrdin, I.N. Dolganova, A.S. Kucheryavenko, A.N. Rossolenko, V.V. Tuchin, V.N. Kurlov, M. Skorobogatiy. *Adv. Opt. Mater.*, **8** (18), 2000307 (2020). DOI: 10.1002/adom.202000307
- [24] G.M. Katyba, M. Skorobogatiy, D.G. Melikyants, N.V. Chernomyrdin, A.N. Perov, E.V. Yakovlev, I.N. Dolganova, I.E. Spektor, V.V. Tuchin, V.N. Kurlov, K.I. Zaytsev. *Phys. Rev. Appl.*, **18** (3), 034069 (2022). DOI: 10.1103/PhysRevApplied.18.034069
- [25] Y.H. Lo, R. Leonhardt. *Opt. Express*, **16** (20), 15991 (2008). DOI: 10.1364/OE.16.015991
- [26] N.C.J. Van Der Valk, P.C.M. Planken. *Appl. Phys. Lett.*, **81** (9), 1558 (2002). DOI: 10.1063/1.1503404
- [27] A.J. Huber, F. Keilmann, J. Wittborn, J. Aizpurua, R. Hillenbrand. *Nano Lett.*, **8** (11), 3766 (2008). DOI: 10.1021/nl802086x
- [28] N.V. Chernomyrdin, A.S. Kucheryavenko, G.S. Kolontaeva, G.M. Katyba, I.N. Dolganova, P.A. Karalkin, D.S. Ponomarev, V.N. Kurlov, I.V. Reshetov, M. Skorobogatiy, V.V. Tuchin,

- K.I. Zaytsev. Appl. Phys. Lett., **113** (11), 111102 (2018).
DOI: 10.1063/1.5045480
- [29] N.V. Chernomyrdin, M. Skorobogatiy, D.S. Ponomarev, V.V. Bukin, V.V. Tuchin, K.I. Zaytsev. Appl. Phys. Lett., **120** (11), 110501 (2022). DOI: 10.1063/5.0085906
- [30] N.V. Chernomyrdin, M. Skorobogatiy, A.A. Gavidush, G.R. Musina, G.M. Katyba, G.A. Komandin, A.M. Khorokhorov, I.E. Spektor, V.V. Tuchin, K.I. Zaytsev. Optica, **8** (11), 1471 (2021). DOI: 10.1364/OPTICA.439286
- [31] M.A. Duguay, Y. Kokubun, T.L. Koch, L. Pfeiffer. Appl. Phys. Lett., **49** (1), 13 (1986). DOI: 10.1063/1.97085
- [32] Z. Zhu, T. Brown. Opt. Express, **10** (17), 853 (2002). DOI: 10.1364/OE.10.000853
- [33] K.I. Zaytsev, G.M. Katyba, V.N. Kurlov, I.A. Shikunova, V.E. Karasik, S.O. Yurchenko. IEEE Trans. Terahertz. Sci. Technol., **6** (4), 576 (2016). DOI: 10.1109/TTHZ.2016.2555981
- [34] N.V. Chernomyrdin, V.A. Zhelnov, A.S. Kucheryavenko, I.N. Dolganova, G.M. Katyba, V.E. Karasik, I.V. Reshetov, K.I. Zaytsev. Opt. Eng., **59** (06), 061605 (2019). DOI: 10.1117/1.oe.59.6.061605
- [35] G.M. Katyba, K.I. Zaytsev, I.N. Dolganova, I.A. Shikunova, N.V. Chernomyrdin, S.O. Yurchenko, G.A. Komandin, I.V. Reshetov, V.V. Nesvizhevsky, V.N. Kurlov. Progress in Crystal Growth and Characterization of Materials, **64** (4), 133 (2018). DOI: 10.1016/j.pcrysgrow.2018.10.002
- [36] A.A. Bushunov, M.K. Tarabrin, V.A. Lazarev. Laser Photon. Rev., **15** (5), 2000202 (2021). DOI: 10.1002/LPOR.202000202

Translated by Ego Translating